Published in final edited form as:
J Mol Biol. 2013 July 24; 425(14): 2529–2540. doi:10.1016/j.jmb.2013.04.007.

Surface for Catalysis by Poliovirus RNA-Dependent RNA Polymerase

Jing Wang[a,1], **John M. Lyle**[b,2], and **Esther Bullitt**[a]

[a]Dept. of Physiology & Biophysics, Boston Univ. School of Medicine, 700 Albany Street, Boston, MA 02118

[b]Dept. of Microbiology & Immunology, Stanford University School of Medicine, 299 Campus Drive, Stanford, CA 94301

Abstract

The poliovirus RNA-dependent RNA polymerase, 3Dpol, replicates the viral genomic RNA on the surface of virus-induced intracellular membranes. Macromolecular assemblies of 3Dpol form linear array of subunits that propagate along a strong protein-protein interaction called interface-I, as was observed in the crystal structure of wild-type poliovirus polymerase. These "filaments" recur with slight modifications in planar sheets and, with additional modifications that accommodate curvature, in helical tubes of the polymerase, by packing filaments together via a second set of interactions. Periodic variations of subunit orientations within 3Dpol tubes give rise to "ghost reflections" in diffraction patterns computed from electron cryomicrographs of helical arrays. The ghost reflections reveal that polymerase tubes are formed by bundles of 4–6 interface-I filaments, which are then connected to the next bundle of filaments with a perturbation of interface interactions between bundles. While enzymatically inactive polymerase is also capable of oligomerization, much thinner tubes are formed that lack interface-I interactions between adjacent subunits, suggesting that long-range allostery produces conformational changes that extend from the active site to the protein-protein interface.

Macromolecular assemblies of poliovirus polymerase show repeated use of flexible interface interactions for polymerase lattice formation, suggesting that adaptability of polymerase-polymerase interactions facilitates RNA replication. In addition, the presence of a positively charged groove identified in polymerase arrays may help position and stabilize the RNA template during replication.

Keywords

helical reconstruction; ghost reflection; membrane; oligomerization; cryo-electron microscopy

---

Corresponding Author: Esther Bullitt. bullitt@bu.edu, T: +1-617-638-5037, F: +1-617-638-4041.
[1] Present address: Dept. of Cell Biology, Yale University, 333 Cedar Street, New Haven, CT 06520
[2] Present address: Pacific Biosciences, 1380 Willow Rd. Menlo Park, CA 94025

Introduction [1]

Evidence for the importance of poliovirus polymerase oligomerization was provided by experiments showing that RNA binding to 3Dpol was highly cooperative [1], indicating that 3Dpol oligomerization facilitates the efficient binding of an RNA template by utilizing co-localization of polymerases into replication factories, as proposed by Cook [2]. In addition, poliovirus replication within infected cells is disrupted by mutation of residues critical for oligomerization of the poliovirus-encoded RNA-dependent RNA polymerase[3; 4]. Although oligomerization of 3Dpol was demonstrated by protein cross-linking [5], yeast two-hybrid screening [6] and directly visualized by electron microscopy [7], the structural details of oligomer formation remain elusive. All RNA viruses studied to date replicate on intracellular membranes [8], and therefore the existence of a planar lattice as the catalytic unit is an attractive concept for membrane-associated RNA replication. The planar lattice of poliovirus 3Dpol observed by EM has been suggested to coat intracellular membranes in infected cells through its interaction with a virus-encoded membrane protein, 3AB [9; 10; 11]. One interface potentially involved in 3Dpol lattice formation was initially identified by crystallographic studies of the wild type polymerase [12]. Contacts across the interface designated as “interface-I” occupy a large surface area, allowing 3Dpol molecules to extend one dimensionally head-to-tail, forming a linear array. The molecules are oriented up and down alternately along the filament axis, so that the asymmetric unit (the unit that repeats) is a 3Dpol dimer. Residues identified as participating in interface-I contacts are critical for both lattice formation and virus growth [3; 4; 13; 14]. Interface-I filaments within the crystal interacted at an oblique angle, forming contacts that occupied less surface area, do not extend the polymerases into a planar lattice, and were not expected to be physiological [12].

Here we characterize the self-assembly of 3Dpol using cryo-electron microscopy and image processing. When incubated at a temperature supporting polymerase activity, macromolecular assemblies of wild type 3Dpol form both planar and helical arrays with similar lattice arrangements, using an interface-I dimer as the asymmetric unit. Polymerases containing the mutation D328A/D329A in the polymerase catalytic center abrogate interactions along interface-I, resulting in the formation of narrow tubes with a monomeric repeating unit [15]. A very similar structure was seen for wild type polymerase oligomerized at a temperature that does not support replication (4° C). The resulting narrow tubes suggest a long-range allosteric conformational change, as described previously [16], that may provide insight into the enzymatic cycle.

Results

Lattice arrangement in a 3Dpol planar lattice

Freshly purified 3Dpol was capable of oligomerizing as a ribbon-like lattice (Fig. 1A). One flat region of such an oligomer showing visible diffraction spots to 20 $Å^{-1}$ was analyzed to provide a projection view of the planar lattice. As seen in Fig. 1B, the unit cell dimensions were a=53Å, b=87Å, $\gamma=89^{\circ}$, confining two blobs of density. Since one 3Dpol monomer is a spheroid of approximately 50 Å diameter, the two blobs contained within one asymmetric unit should correspond to two polymerase molecules. As shown by the weak reflections resembling systematic absences along the y-axis at positions corresponding to 2n+1, the symmetry of the projection is pseudo-$p2_1$, indicating that the molecules composing each asymmetric unit are connected head-to-tail with a rotation of 180°. The resulting “up and down” alternating arrangement of densities along a 2_1 screw axis is very similar to the

---

[1] *Abbreviations*: EM, electron microscopy; 3Dpol, poliovirus polymerase protein 3D; 3-D, three-dimensional; MWCO, molecular weight cut off; CCD, charge-coupled device. CTF, contrast transfer function

interface-I pattern observed in the 3-D crystals of poliovirus wild type polymerase (Fig. 1c–d). In the perpendicular direction, which we propose to be the interface-II connection, 3Dpol molecules simply repeat themselves by a translation of 53 Å without additional rotation. Thus, interface-I filaments are arranged in a parallel manner by this interface-II connection in the planar arrays.

Notably, the pair of 3Dpol molecules within an asymmetric unit are non-equivalent (Fig. 1c), with one of them showing a stronger density and a less well-defined boundary. These strong/weak densities could have been caused by artifacts of negative staining, since molecules with the alternating up-down orientations could have trapped stain differently. However, as shown below, cryo-electron cryomicroscopy data from helical tubes of 3Dpol recapitulate this alternating pattern of densities, consistent with the structure determined for the planar lattice. Differences between the two polymerases within one asymmetric unit gave rise to variations in the strength of both interface-I and interface-II contacts. This resulted in slightly modified interface-I contacts within the unit cell as compared to interface-I contacts between unit cells. Consequently, there were distinguishable interface-II interactions between adjacent 3Dpols, seen as interactions between two weak-density or two strong-density polymerases. These interactions were propagated throughout the planar lattice.

Packing of 3Dpol in tubular arrays

Formation of tubes—Purified polymerase more than one day old predominantly formed helical arrays when oligomerized at 30°C, possibly due to degradation or dissociation of a contamination co-purified with the polymerase. When incubated at 4°C only, monomeric 3Dpol oligomerized as narrow filaments (“cold filaments”) approximately 100 Å in diameter (Fig. 2A). Following incubation for five minutes at a temperature that supports RNA synthesis (30 °C), short tubes with wider diameters (500 Å) and ribbons that appeared to be rolling into tubes were observed (Supplementary Fig. 1). A longer incubation time (30 min) produced longer tubular arrays (0.5 μm to 3 μm), while their width remained fairly constant at 300–700 Å. “Cold filaments” of wild type polymerase were morphologically indistinguishable (at the current resolution) from tubes of the active-site mutant polymerase YGAA assembled at 30 °C, as seen in Fig. 2D, and modeled in Fig. 2C. To show the similarites, Fourier transforms of a modeled tube, a straightened YGAA tube, and a cold filament are shown in Fig. 2 E, F, G, respectively.

Helix indexing—Cryo electron microscopy images of 3Dpol tubes, such as the one shown in Fig. 3A were used to compute diffraction patterns to investigate the nature of the periodicities observed in the images. Helical symmetry gives rise to a series of horizontal lines symmetric about the meridian (y-axis). These lines (“layer lines”) are the hallmark of helical diffraction patterns, indicating that 3Dpol tubular arrays were helical. Although the diffraction patterns from tubular arrays were different from those of planar arrays, the unit cell defined by the maxima on the layer lines and the corresponding reflection peaks was similar (Supplementary Fig. 2). These data indicated that the helical arrays were formed by rolling up the planar arrays into a hollow cylinder, so that 3-D reconstruction of helical arrays would also provide structural information about planar arrays of 3Dpol. The diffraction pattern shown in Fig. 3B is from a family of tubes that was characterized by two principal helices, a 31-start left-handed helix and a 6-start right-handed helix, and the range of helical symmetries for all tubes that were analyzed is quantified in the Supplementary Table. The diffraction pattern in Fig. 3B was classified as a (−31, 6) helix denoted by (1, 0; −31) and (0, 1; 6) using h, k and n indices [17] and a negative sign to denote a left-handed helix. Notably, the 25-start helix (1, 1; −25) gave rise to a much stronger layer line than the 31-start helix originally indexed as the (1, 0) principal helix. Because cryo-EM images have very low contrast, these patterns are not easily visible in individual images. Helical families are most clearly visualized on the reconstruction shown in Fig. 4A, from tubes of the (−32, 6) family showing strong 26-start and 6-start helices. The unit cell dimensions defined by (1, 0) and (1, 1) layer lines in the tubular array shown in Fig. 3 (a= 90Å, b= 47Å, γ=82°) are very similar to those of the 3Dpol planar array (a= 87Å, b= 53Å, γ=89°). The unit cell dimension (a=87Å) also correspond well with the 88Å interface-I unit cell dimension of 3Dpol crystals, as measured by x-ray crystallography [12]. Therefore, we suspect that the interface-I dimer propagated along the 25-start helix in this (−31,6) tube; note that the 25-start helix is aligned in a manner perpendicular to the 6-start helix.

Identification of ghost reflections—A striking feature of the 3Dpol tube diffraction patterns was the appearance of “forbidden reflections” or “ghost reflections” [18] convoluted with the regular helical layer lines. Ghost reflections in this diffraction pattern were coupled to the regular helical lattice lines, offset from their nearby layer line maxima by (x, n_x) along the (1, 1) direction. Additional layer lines that would denote a simple increase in the unit cell size were not observed. This effect was also not due to flattening of tubes, as this would lead to changes in the position of diffraction maxima along layer lines, not addition of new layer lines.

Visible layer lines corresponding to (0, 1+x; 6+n_x), (0, 2+x; 12+n_x) and (1, 3+x; −13+n_x) were observed in the transforms of all tubes analyzed, where x is 1/4 to 1/6 the spacing of (1, 1), and correspondingly n_x is 1/4 to 1/6 of the Bessel order $n_{1,\,1}$. The precise value of n_x varied for different helical families. The computed Fourier transform of a (−31, 6) class 3Dpol tube is shown in Fig. 3B. For the tube shown in Fig. 3, the spacing from ghost reflections to the maxima of nearby regular layer lines was one-fifth of the (1, 1; −25) vector length, so that $n_x = -5$. Ghost reflections thus appeared at layer lines (0, 1+ 1/5; 1), (0, 2+ 1/5; 7) and (1, 3+ 1/5; −18). In real space, the underlying regular helical array was disturbed by a function with a periodicity five times larger than that for a strict helical symmetry of (1, 1; −25). The distance to the (1, 1) position corresponded with the dimension of one polymerase, so we expect that the ghost reflections were derived from local perturbation of every 5 polymerases along the (1, 1) direction, giving rise to a super lattice that coupled sequential rotations and minor conformational changes of 5 polymerases with the primitive helical lattice, before repeating the first polymerase orientation and conformation.

Interfaces revealed in tubular arrays of 3Dpol—As shown in Fig. 4A, the 3-D structure of the (−32, 6) family of 3Dpol tubes was reconstructed using conventional Fourier-Bessel methods for helical structures [19; 20]. The resolution of the reconstruction is 16 Å. Similar to the projection map of 3Dpol planar arrays, the asymmetric unit of the primitive helical arrays (reconstructed without ghost reflections) contained two blobs with different density profiles shown in Fig. 4B. Two monomers from the complete crystal structure of 3Dpol (PDB 1ra6) were placed along interface-I as defined by the wild type 3Dpol crystal structure (PDB 1rdr) and denoted as the “interface-I dimer”. This dimer was then fitted into the volume of the EM density map from the helical reconstruction. With slight bending between adjacent asymmetric units, interface-I dimers were propagated along a 26-start helix as seen in Fig. 4C. Thus, interface-I interactions within a unit cell and between adjacent unit cells were similar but not identical, resulting in two slightly different interface-I interactions (within and between asymmetric units) for both planar arrays and helical tubes of 3Dpol. The 26-start helical strands were held together side-by-side via interface-II interactions, which also alternated in strength, producing two types of interface-II (Fig. 4D). Residues whose mutation disrupted 3Dpol lattice formation [21], including Y32 and S438, were localized at the interface-II as determined by fitting the atomic structure of wild type 3Dpol into the helical reconstruction of 12,000 subunits from 7 tubes. Interface-II interactions between the upper two polymerases shown in Fig. 4D were much weaker, involving only two residues, Y32 and D459 (Fig. 4E). Strong interface-II contacts involving 19 residues were observed between the lower two polymerases. N- and C-terminal residues of the dark blue molecule (K22, D26, P27, S28, H31 and Y32 from the N-terminal finger domain; W403, S438, V440 and R443 from the C-terminal thumb domain) constitute the finger contacts of interface-II. Residues P222, V223, L224, M225, D226, H320 and F386 of the light blue molecule constitute the palm contacts of interface-II (Fig. 4F).

Ghost reflections further modify interface-I and interface-II—Including the ghost layer lines for the 3-D reconstruction resulted in a super unit cell along the (1, 1) direction that included density sufficient to accommodate ten polymerase molecules. Consequently, ten different conformations for each interface were observed in the reconstructed 3Dpol tube of a (−31, 6) family member, indicating that polymerase molecules are not entirely immobilized within the lattice. Instead, each is capable of slightly dislocating from its “crystalline” position. As shown in Fig. 5A, five copies of the interface-I dimer were fitted side by side into one such super unit cell. Each copy turned slightly sideways as compared to its fit into the regular helical structure. As a result, a gap was introduced between every group of five 25-start helical strands, when the orientation of the subunits repeated.

Interface-I, modified by ghost reflections—To examine the contacts between polymerase molecules we used an interface-I dimer of the wild type 3Dpol structure[12] (described above) for fitting into our EM map reconstructed including ghost layer lines. This dimer has an approximately cylindrical shape 47 Å in diameter and 90 Å in length, matching the unit cell size of the polymerase tube. The organization of two blobs of density related by a pseudo-2_1 screw axis allowed fitting the known interface-I dimer into the EM-density map with a moderate degree of accuracy (cross-correlation =0.88 to 0.91), despite the 25 Å resolution of this map and the expected functional mobility of subunits in the oligomeric structure. To illustrate this fitting, in Fig. 5C, a pair of interface-I dimers docked into the reconstruction is shown in cross section along a 25-start helix. Variations of interface-I were evaluated by comparing the five distinct interface-I contacts between adjacent unit cells. These contact residues are listed in table 1.

Interface-II, modified by ghost reflections—Interactions along interface-II were initially evaluated by fitting the full-length structure of 3Dpol (PDB 1ra6) into 6-start helical strands of both the primitive helical lattice and the reconstruction that included ghost reflections as seen in Fig. 5B,D. The fingers domain appeared to make extensive interactions and clashes between adjacent 3Dpol molecules at the stronger interface-II contact, suggesting the fingers domain assumes an alternate conformation from the conformation determined by X-ray crystallography for interface-I mutant polymerases [22]. It is expected that the fingers domain remains disordered in the helical lattice, as it does in the wild type polymerase 3-D crystals [12]. This assumption is supported by the lack of visible density for fitting of the fingers domain at the interface-II connection. It is possible, however, that a large conformational change of the fingers domain causes it to swing towards the extra density visible in the EM map, as seen in Fig. 5E. Interface-II contacts are shown in table 2, as defined by fitting pairs of interface-I dimers from the partial structure of 3Dpol into the EM map and searching for residues that make direct contacts along the 6-start helical strand. Additional contacts that involve the fingers domain are expected, but these contacts cannot be reliably predicted at the current resolution of our reconstruction.

Analysis of a catalytically inactive 3Dpol tube—The catalytic site of RNA-dependent RNA polymerases contains a highly conserved YGDD amino acid motif in the palm domain [12; 23]. To assess the role of 3Dpol oligomerization during RNA replication, the structure of a macromolecular array of catalytically inactive 3Dpol^{YGAA} (D328A, D329A) was analyzed by electron microscopy. $3\text{Dpol}^{\text{YGAA}}$ oligomerized after incubation at 30 °C formed a 100Å diameter narrow filament [15] as shown in Fig. 2B, surprisingly similar to the wild type cold filament (Fig. 2A). Helical symmetry of both the $3\text{Dpol}^{\text{YGAA}}$ and wild type 3Dpol cold filaments indicated that the dimensions of each asymmetric unit of the helical lattice is 47Å by 55Å, and therefore can accommodate only one polymerase molecule (Fig. 2G). Specifically, as a result of the lack of $P2_1$ symmetry, no interface-I connection is possible in these lattices. Because inactive enzymatic mutants of 3Dpol are inaccessible to antibodies against the active site [23], we suspect the mutant polymerase captured a tight conformation of the wild type 3Dpol in filaments assembled at cold temperatures that do not support RNA synthesis.

Discussion

From plane to helix, 3Dpol lattices maintained interface-I dimers as their constituent unit cell after incubation at a temperature that supports replication. A distortion was observed after every 4 to 6 polymerase molecules in helical tubes of 3Dpol. This distortion is expected to relax accumulated tension built up during bending of the flat lattice into a tube. Thus, the variation of polymerase-polymerase interfaces determined by our reconstructions is derived from dynamic properties of molecules within the lattice that accumulate and release strain, and is expected to account for our inability to observe 3Dpol two-dimensional crystals and helical crystals that diffract to high resolution. Functionally, we expect this flexibility to enable 3Dpol lattices to accommodate diverse curvature such as that found on membranes of virus-induced vesicles 50–400 nm in diameter in infected cells [24; 25]. Membrane binding of 3Dpol is via the membrane-associated protein 3AB. Following the alternating pattern of 3Dpol lattice, the 3AB binding site on 3Dpol [9; 26], shown in Supplementary Fig. 4, is oriented such that either side of the planar array could bind to the membrane.

Microtubules are helical tubes that also accommodate seams [27]. Most commonly, each microtubule has a single seam, and the lateral interactions shift from α to α tubulin subunits to an interaction between an α- and a β-tubulin [28]. Thus, in contrast to polymerase tubes, the microtubule seam occurs by one whole-subunit translation along the protofilament. Conversely, the subunits in tubes of 3Dpol show much more flexibility, which results in many conformations of the molecule within each tube, and multiple dislocations around the tube at positions where the subunit conformation repeats a conformation 4–6 subunits away. Note that in microtubules, the end-to-end arrangement of subunits along protofilaments is always alternating α,β,α,β… subunits, similar to the up,down,up,down… arrangement of polymerases in 3Dpol tubes.

Interface-I stabilizes a more accessible catalytic site

The asymmetric units of both planar arrays and helical lattices of wild-type 3Dpol consist of two polymerases in contact via interface-I. A slightly modified version of this interface connects adjacent unit cells head-to-tail in these two types of oligomers to produce linear arrays of polymerases with similar subunit-subunit interactions. These interactions have only been observed for wild-type enzyme incubated at a temperature that supports polymerase activity (30 °C). Interface-I was not observed in the catalytically inactive 3Dpol lattice or in wild type 3Dpol lattices formed at low temperature. We therefore confirm the physiological importance of interface-I and note that this interaction corresponds to a conformation specific for active polymerase in which the hydrophobic tip of the thumb domain is exposed and then stabilized by contacting the palm of the neighbor molecule along interface-I. The formation of interface-I contacts may help maintain this more open conformation of the polymerase, facilitating access of nucleotides and RNA template to the enzyme. In contrast, both the active site mutant $3\text{Dpol}^{\text{YGAA}}$ and wild-type 3Dpol oligomerized at low temperature exhibit long-range conformational changes that result in a more closed conformation of the protein. This suggests the possibility that the enzymatic reaction is dependent on mobility of the protein that extends well beyond the active site, and that inactive 3Dpol may maintain a conformation that folds the thumb and fingers domain towards the palm domain, blocking access to the catalytic center.

Interface-II provides a path for RNA binding

It appears that interface-I contacts play the primary role in holding polymerases within the helical lattice. Interface-II contacts are not extensive, so we expect the region of the polymerase near interface-II to be more flexible, resulting in the observed weaker densities in the final reconstructed maps. Interface-II does, however, include attributes that would facilitate RNA binding. An RNA binding path within the helical lattice was estimated initially by aligning the structure of the PV 3Dpol RNA elongation complex [29] along interface-I in our EM map. As seen in Fig. 6, Interface-II appears to provide a groove along the helix surface where template RNA might be passed among replicating polymerases, providing cooperativity for RNA binding. Known RNA binding residues (K125, K126, K127, K128, K133, K188 [30]; R455, R456 [11]; L342, L446 [3]) lie along the groove created by interface-II interactions, indicating a channel for binding RNA template. The binding site for the RNA synthesis primer VPg [9; 31; 32; 33; 34] and the catalytic centers of the enzymes hang above the RNA channel, so that another round of RNA synthesis could be initiated immediately after an RNA template passes by. Interestingly, the 3Dpol^{YGAA} oligomer itself is inactive, but is capable of enhancing RNA elongation in vitro when a concentration of wild type 3Dpol which is too low for observable replication is present [15]. Interface-II contacts may be maintained by 3Dpol^{YGAA}, keeping adjacent 3Dpols in register to facilitate RNA binding. Thus wild type 3Dpol below the minimal concentration for RNA synthesis regains its activity in the presence of 3Dpol^{YGAA}. Notably, interface-II mutations failed to supplement RNA synthesis by wild type polymerase, whereas interface-I mutations did not significantly affect the stimulatory effect of YGAA mutant polymerases [15]. These data support the importance of interface-II for efficient RNA binding.

Parallel Planar Arrays

Our experimental data show that adjacent interface-I fibers are oriented parallel to each other in both helical arrays and planar arrays of 3Dpol. This is in contrast to our recent molecular dynamics study, which suggested interface-I fibers composing a planar array were arranged in an anti-parallel orientation [21]. Parallel models were excluded in an early step of computational modeling, since extension of tetramers with repeating subunit-subunit contacts gave rise to an open spiral lattice (see Supplementary Fig. 3), rather than a planar array. Because the expectation was that the lattice coating the surface of intracellular membrane was planar, a parallel arrangement of fibers was not further pursued. Moreover, the empirically derived interface-I fiber model requires as many as ten interface-I interactions and ten interface-II interactions. Such complexity could not be computationally modeled in our molecular dynamics system, and was not reasonable to assume with no experimental data to support it. The current results demonstrate that parallel lattices of 3Dpol can assume both flat and helical configurations, suggesting that conformational changes at interface-I and interface-II, or slightly altered subunit-subunit contacts are tolerated (and necessary) for formation of these arrays.

Role of PV 3Dpol oligomerization

Self-assembly of polymerases has been shown for various RNA viruses, such as HCV [35; 36] norovirus [37], foot and mouse disease virus [38; 39] and HRV-14 [40], suggesting that oligomerization is a common feature of RNA-dependent RNA polymerases. The RNA genome of poliovirus is translated as a single polyprotein that is variably processed into stable intermediates and final products. As such, more copies of the polymerase are produced than is necessary for replication. Some 3Dpol molecules generated during the polyprotein processing serve additional roles, including structural support for assembly of RNA replication complexes [15]. Due to the pseudo $P2_1$ symmetry of 3Dpol in its active, oligomerized state, half of the polymerases within the lattice would be facing the membrane and the other half would be facing the cytosol. Those 3Dpol subunits with their active sites inaccessible to the cytosolic milieu appear to be providing a structural role. We cannot, however, exclude the possibility that redundant polymerases on intracellular membranes are simply sequestered there, not directly benefitting virus replication, but merely accommodating the surplus polymerase associated with viral polyprotein expression.

The observed oligomerization of poliovirus 3Dpol appears to be a common feature for virus-encoded RNA polymerases. Therefore, a continued investigation of the structural basis for self-assembly of viral RNA dependent RNA polymerases may identify new targets for antiviral therapy.

Materials and Methods

3Dpol expression and purification

An expression plasmid for full-length 3Dpol pT5T-3D was provided by Dr. Karla Kirkegaard [1]. 3Dpol expression in BL21(DE3)-pLysS cells transformed with pT5T-3D was induced with IPTG 0.5 mM for 16 hr at 25 °C. All subsequent steps were carried out at 4 °C. Cells were harvested by centrifugation at 4000 x g for 15 min and then lysed by sonication in breaking buffer (100 mM Na_2HPO4 pH 7.5, 0.1 mM EDTA, 2 mM DTT, 0.02% NaN_3). Lysate was clarified at 20,000 x g for 30 min. Protein was precipitated with 40% ammonium sulfate, followed by centrifugation at 20,000 x g for 30 min to collect the protein precipitate. The pellet was suspended in 40 ml dialysis buffer (25 mM Tris pH 7.5, 50 mM NaCl, 0.02% NaN_3, 0.1 mM EDTA, 2 mM DTT) and dialyzed against 2 L of the same buffer overnight using Spectra-pore membrane with 3.5K MWCO. Glycerol was added to the cleared dialysate supernatant to a final concentration of 15% and the sample was then purified by S-sepharose (Biorad) cation-exchange chromatography using buffer S (50 mM Tris pH 8.5, 0.02% NaN_3, 0.2 mM EDTA, 15% glycerol, 0.5% β-OG, 2 mM DTT), followed by Q-sepharose (Bio-Rad) ion-exchange chromotagraphy using buffer Q (25 mM Tris pH 8.0, 0.02% NaN_3, 15% glycerol, 0.5% β-OG, 2 mM DTT.). Purified proteins were mixed with 100% glycerol at 1:1 volume ratio, flash frozen in liquid nitrogen and stored at −80°C up to 6 months.

3Dpol oligomerization assay

Frozen protein stock was thawed on ice for 10 min and then spun to 14,000 x g for one second to pellet potential protein aggregates. A 10 μl aliquot of 3Dpol was diluted into 50 μl TE buffer (10 mM Tris pH 7.5, 1 mM EDTA pH 8.0) on ice for 10 min, incubated 30 min at 30 °C, and then kept at room temperature (RT) for 2–6 hr. Before plunge-freezing, the sample was transferred into a 50 μl dialysis button (Hampton Research), sealed with dialysis membrane at 12,000–14,000 MWCO and dialyzed against TE30 (10 mM Tris pH 7.5, 1 mM EDTA pH 8.0, 30 mM NaCl) at RT for 30 min to remove glycerol.

Electron microscopy

For negative stain, sample was applied to a continuous-carbon coated grid, washed with TE buffer and then stained using 1% uranyl acetate. For cryo-EM, sample was applied to freshly glow discharged Quantifoil® 1.2/1.3 holey carbon grids, blotted and vitrified using a Vitrobot from FEI. The chamber temperature was maintained at 20 °C and the humidity was kept at 100% during the blotting process. Grids were transferred to a Gatan70 cryo-holder cooled by liquid nitrogen and loaded into a Tecnai F20 electron microscope (FEI), which was aligned at an accelerating voltage of 160 keV. A defocus ranging from −1.5 to −2.5 μm was randomly set and the micrographs were recorded at 29,000 x magnification with a 4K CCD camera (TVIPS), resulting in an effective pixel size of 2.9 Å on the specimen scale. The electron dose for each image was maintained at approximately $20e^{-1}$/Å to limit radiation damage.

Image processing by EMIP (EM Imaging Processing)

A two-dimensional projection map of the 3Dpol planar array was obtained using the 2dx software package [41]. The EMIP (EM Imaging Processing) software [42] was used for helical reconstruction of 3Dpol tubes. Individual tubes were indexed after correction for in-plane rotation, helical axis shift and out-of-plane tilt. Tubes of the same symmetry were corrected for CTF using CTFFIND3 [43], aligned to the same phase origin and averaged in Fourier space. The resolution of a dataset was estimated by checking the phase quality of the averaged layer line data. Flat phases along the peaks of layer line maxima are a signature of helical diffraction, thus they were used to determine whether a layer line contained signal above the background noise level. Visible ghost layer lines were extracted and included into the 3-D reconstruction using the MRC package [44].

Fitting of atomic models into the EM-density map

Interface-I dimers defined by crystal packing of wild type 3Dpol atomic structure (PDB 1rdr) were used as reference to superimpose two copies of the full-length structure of 3Dpol mutant (PDB 1ra6) so that they maintained the original interface-I contact. The cutoff level that gave a volume corresponding to the known mass of reconstructed 3Dpol tube was estimated based on a protein density of 1.23 $Å^3$/Da. The volume of the 3Dpol reconstruction map was estimated by $2x(\text{z-length}/\Delta z) \times MW^{3Dpol} \times 1.23\ Å^3/Da$ [45], where z-length is the axial length of the final reconstructed 3Dpol map, 300 Å; Δz is the rise/asymmetric unit, ~6 Å; and MW^{3Dpol} is the molecular weight of the 3Dpol, ~52 kDa. The isosurface level of the EM map used for fitting was adjusted until the map volume matched the estimated volume. The whole interface-I dimer as the asymmetric unit of the 3Dpol helical array was initially placed manually into the EM-density map The built-in function *fit in map* of UCSF Chimera [46] was then run to find the best fitting of the atomic structure of the 3Dpol dimer into the EM density map. The “find clash/contact” program was run during the fitting to ensure there were no steric clashes between adjacent polymerases.

Image processing by 2dx

One rectangular segment from a negatively stained 3Dpol planar array that was capable of diffracting to 20 Å was used to compute a two-dimensional projection map. The lattice arrangement was initially determined from the diffraction pattern of the whole micrograph. Strong and sharp diffraction spots were back-transformed as a reference image for unbending. The cross-correlation (cc) map between reference and the input image was then used to identify best area of the original micrograph containing single-layered, highly ordered 2d crystal. Reflections were boxed from the diffraction pattern of the masked image and were used to generate the final map.

Supplementary Material

Refer to Web version on PubMed Central for supplementary material.

Acknowledgments

We are most grateful to Dr. Karla Kirkegaard for helpful discussion and critical reading the manuscript. We also thank Dr. Christopher Akey, Dr. Donald Caspar, and Dr. Nikolaus Grigorieff for suggestions on electron microscopy and data analysis. This work was supported by BUSM and NIH/NIGMS GM102474. EM maps have been deposited in the EMDB, 11327 and 26566.

References

1. Beckman MT, Kirkegaard K. Site size of cooperative single-stranded RNA binding by poliovirus RNA-dependent RNA polymerase. J Biol Chem. 1998; 273:6724–6730. [PubMed: 9506971]
2. Cook PR. The organization of replication and transcription. Science. 1999; 284:1790–1795. [PubMed: 10364545]
3. Hobson SD, Rosenblum ES, Richards OC, Richmond K, Kirkegaard K, Schultz SC. Oligomeric structures of poliovirus polymerase are important for function. Embo J. 2001; 20:1153–1163. [PubMed: 11230138]
4. Pathak HB, Ghosh SKB, Roberts AW, Sharma SD, Yoder JD, Arnold JJ, Gohara DW, Barton DJ, Paul AV, Cameron CE. Structure-function relationships of the RNA-dependent RNA polymerase from poliovirus (3Dpol). A surface of the primary oligomerization domain functions in capsid precursor processing and VPg uridylylation. J Biol Chem. 2002; 277:31551–31562. %W http://view.ncbi.nlm.nih.gov/pubmed/12077141. [PubMed: 12077141]
5. Pata JD, Schultz SC, Kirkegaard K. Functional oligomerization of poliovirus RNA-dependent RNA polymerase. RNA. 1995; 1:466–477. [PubMed: 7489508]
6. Xiang W, Cuconati A, Hope D, Kirkegaard K, Wimmer E. Complete protein linkage map of poliovirus P3 proteins: interaction of polymerase 3Dpol with VPg and with genetic variants of 3AB. J Virol. 1998; 72:6732–6741. [PubMed: 9658121]
7. Lyle JM, Bullitt E, Bienz K, Kirkegaard K. Visualization and functional analysis of RNA-dependent RNA polymerase lattices. Science. 2002; 296:2218–2222. %W http://view.ncbi.nlm.nih.gov/pubmed/12077417. [PubMed: 12077417]
8. Schlegel A, Giddings TH Jr. Ladinsky MS, Kirkegaard K. Cellular origin and ultrastructure of membranes induced during poliovirus infection. J Virol. 1996; 70:6576–6588. [PubMed: 8794292]
9. Hope DA, Diamond SE, Kirkegaard K. Genetic dissection of interaction between poliovirus 3D polymerase and viral protein 3AB. J Virol. 1997; 71:9490–9498. [PubMed: 9371611]
10. Lama J, Paul AV, Harris KS, Wimmer EJ. Properties of purified recombinant poliovirus protein 3aB as substrate for viral proteinases and as co-factor for RNA polymerase 3Dpol. J. Biol. Chem. 1994; 269:66–70. %W http://www.jbc.org/cgi/content/abstract/269/1/66. [PubMed: 8276867]
11. Lyle JM, Clewell A, Richmond K, Richards OC, Hope DA, Schultz SC, Kirkegaard K. Similar structural basis for membrane localization and protein priming by an RNA-dependent RNA polymerase. J Biol Chem. 2002; 277:16324–16331. %W http://view.ncbi.nlm.nih.gov/pubmed/11877407. [PubMed: 11877407]
12. Hansen JL, Long AM, Schultz SC. Structure of the RNA-dependent RNA polymerase of poliovirus. Structure. 1997; 5:1109–1122. [PubMed: 9309225]
13. Diamond SE, Kirkegaard K. Clustered charged-to-alanine mutagenesis of poliovirus RNA-dependent RNA polymerase yields multiple temperature-sensitive mutants defective in RNA synthesis. J Virol. 1994; 68:863–876. [PubMed: 8289389]
14. Burgon TB, Jenkins JA, Deitz SB, Spagnolo JF, Kirkegaard K. Bypass suppression of small-plaque phenotypes by a mutation in poliovirus 2A that enhances apoptosis. J Virol. 2009; 83:10129–10139. [PubMed: 19625405]
15. Spagnolo JF, Rossignol E, Bullitt E, Kirkegaard K. Enzymatic and nonenzymatic functions of viral RNA-dependent RNA polymerases within oligomeric arrays. Rna. 2010; 16:382–393. [PubMed: 20051491]
16. Boerner JE, Lyle JM, Daijogo S, Semler BL, Schultz SC, Kirkegaard K, Richards OC. Allosteric effects of ligands and mutations on poliovirus RNA-dependent RNA polymerase. J Virol. 2005; 79:7803–7811. [PubMed: 15919933]

17. Toyoshima C, Unwin N. Three-dimensional structure of the acetylcholine receptor by cryoelectron microscopy and helical image reconstruction. J Cell Biol. 1990; 111:2623–2635. [PubMed: 2277076]
18. Caspar DL, Holmes KC. Structure of dahlemense strain of tobacco mosaic virus: a periodically deformed helix. J Mol Biol. 1969; 46:99–133. [PubMed: 5358645]
19. DeRosier DJ, Moore PB. Reconstruction of three-dimensional images from electron micrographs of structures with helical symmetry. J Mol Biol. 1970; 52:355–369. [PubMed: 5485914]
20. Allen GS, Wu CC, Cardozo T, Stokes DL. The architecture of CopA from Archeaoglobus fulgidus studied by cryo-electron microscopy and computational docking. Structure. 2011; 19:1219–1232. [PubMed: 21820315]
21. Tellez AB, Wang J, Tanner EJ, Spagnolo JF, Kirkegaard K, Bullitt E. Interstitial Contacts in an RNA-Dependent RNA Polymerase Lattice. J Mol Biol. 2011; 412:737–750. [PubMed: 21839092]
22. Thompson AA, Peersen OB. Structural basis for proteolysis-dependent activation of the poliovirus RNA-dependent RNA polymerase. EMBO J. 2004; 23:3462–3471. %W http://view.ncbi.nlm.nih.gov/pubmed/15306852. [PubMed: 15306852]
23. Jablonski SA, Morrow CD. Mutation of the aspartic acid residues of the GDD sequence motif of poliovirus RNA-dependent RNA polymerase results in enzymes with altered metal ion requirements for activity. J Virol. 1995; 69:1532–1539. [PubMed: 7853486]
24. Bienz K, Egger D, Pfister T, Troxler M. Structural and functional characterization of the poliovirus replication complex. J Virol. 1992; 66:2740–2747. [PubMed: 1313898]
25. Suhy DA, Giddings TH Jr. Kirkegaard K. Remodeling the endoplasmic reticulum by poliovirus infection and by individual viral proteins: an autophagy-like origin for virus-induced vesicles. J. Virol. 2000; 74:8953–8965. [PubMed: 10982339]
26. Lyle JM, Bullitt E, Bienz K, Kirkegaard K. Visualization and functional analysis of RNA-dependent RNA polymerase lattices. Science. 2002; 296:2218–2222. [PubMed: 12077417]
27. Amos L, Klug A. Arrangement of subunits in flagellar microtubules. J Cell Sci. 1974; 14:523–549. [PubMed: 4830832]
28. Kikkawa M, Ishikawa T, Nakata T, Wakabayashi T, Hirokawa N. Direct visualization of the microtubule lattice seam both in vitro and in vivo. J Cell Biol. 1994; 127:1965–1971. [PubMed: 7806574]
29. Gong P, Peersen OB. Structural basis for active site closure by the poliovirus RNA-dependent RNA polymerase. Proc Natl Acad Sci U S A. 2010; 107:22505–22510. [PubMed: 21148772]
30. Kortus MG, Kempf BJ, Haworth KG, Barton DJ, Peersen OB. A template RNA entry channel in the fingers domain of the poliovirus polymerase. J Mol Biol. 2012; 417:263–278. [PubMed: 22321798]
31. Takegami T, Kuhn RJ, Anderson CW, Wimmer E. Membrane-dependent uridylylation of the genome-linked protein VPg of poliovirus. Proceedings of the National Academy of Sciences of the United States of America. 1983; 80:7447–7451. [PubMed: 6324172]
32. Tellez AB, Crowder S, Spagnolo JF, Thompson AA, Peersen OB, Brutlag DL, Kirkegaard K. Nucleotide channel of RNA-dependent RNA polymerase used for intermolecular uridylylation of protein primer. J Mol Biol. 2006; 357:665–675. [PubMed: 16427083]
33. Lyle JM, Clewell A, Richmond K, Richards OC, Hope DA, Schultz SC, Kirkegaard K. Similar structural basis for membrane localization and protein priming by an RNA-dependent RNA polymerase. J Biol Chem. 2002; 277:16324–16331. [PubMed: 11877407]
34. Strauss DM, Wuttke DS. Characterization of protein-protein interactions critical for poliovirus replication: analysis of 3AB and VPg binding to the RNA-dependent RNA polymerase. J Virol. 2007; 81:6369–6378. [PubMed: 17409142]
35. Chinnaswamy S, Murali A, Li P, Fujisaki K, Kao CC. Regulation of de novo-initiated RNA synthesis in hepatitis C virus RNA-dependent RNA polymerase by intermolecular interactions. J Virol. 2010; 84:5923–5935. [PubMed: 20375156]
36. Clemente-Casares P, Lopez-Jimenez AJ, Bellon-Echeverria I, Encinar JA, Martinez-Alfaro E, Perez-Flores R, Mas A. De novo polymerase activity and oligomerization of hepatitis C virus RNA-dependent RNA-polymerases from genotypes 1 to 5. PLoS One. 2011; 6:e18515. [PubMed: 21490973]

37. Hogbom M, Jager K, Robel I, Unge T, Rohayem J. The active form of the norovirus RNA-dependent RNA polymerase is a homodimer with cooperative activity. J Gen Virol. 2009; 90:281–291. [PubMed: 19141436]

38. Ferrer-Orta C, Sierra M, Agudo R, de la Higuera I, Arias A, Perez-Luque R, Escarmis C, Domingo E, Verdaguer N. Structure of foot-and-mouth disease virus mutant polymerases with reduced sensitivity to ribavirin. J Virol. 2010; 84:6188–6199. [PubMed: 20392853]

39. Bentham M, Holmes K, Forrest S, Rowlands DJ, Stonehouse NJ. Formation of Higher-Order Foot-and-Mouth Disease Virus 3Dpol Complexes Is Dependent on Elongation Activity. J Virol. 2012; 86:2371–2374. [PubMed: 22156531]

40. Love RA, Maegley KA, Yu X, Ferre RA, Lingardo LK, Diehl W, Parge HE, Dragovich PS, Fuhrman SA. The crystal structure of the RNA-dependent RNA polymerase from human rhinovirus: a dual function target for common cold antiviral therapy. Structure. 2004; 12:1533–1544. [PubMed: 15296746]

41. Gipson B, Zeng X, Zhang ZY, Stahlberg H. 2dx--user-friendly image processing for 2D crystals. J Struct Biol. 2007; 157:64–72. %W http://view.ncbi.nlm.nih.gov/pubmed/17055742. [PubMed: 17055742]

42. Diaz R, Rice WJ, Stokes DL. Fourier-Bessel reconstruction of helical assemblies. Methods Enzymol. 2010; 482:131–165. [PubMed: 20888960]

43. Mindell JA, Grigorieff N. Accurate determination of local defocus and specimen tilt in electron microscopy. J Struct Biol. 2003; 142:334–347. [PubMed: 12781660]

44. Crowther RA, Henderson R, Smith JM. MRC image processing programs. J Struct Biol. 1996; 116:9–16. [PubMed: 8742717]

45. Matthews BW. Solvent content of protein crystals. J Mol Biol. 1968; 33:491–497. [PubMed: 5700707]

46. Goddard TD, Huang CC, Ferrin TE. Visualizing density maps with UCSF Chimera. J Struct Biol. 2007; 157:281–287. [PubMed: 16963278]

47. Blestel S, Kervrann C, Chrétien D. A Fourier-based method for detecting curved microtubule centers: Application to straightening of cryo-electron microscope images. Proceedings of the IEEE International Symposium on Biomedical Imaging: From Nano to Macro. 2009:298–301.

Highlights

1. Planar and tubular arrays of poliovirus polymerase have similar subunit contacts.
2. Head-to-tail dimers form the asymmetric unit of wild-type polymerase oligomers.
3. Periodic packing deviations result in ‘ghost’ reflections in diffraction patterns.
4. Data indicate that RNA is stabilized along a lysine-rich groove.
5. Oligomers of polymerase show stability coupled with flexibility.

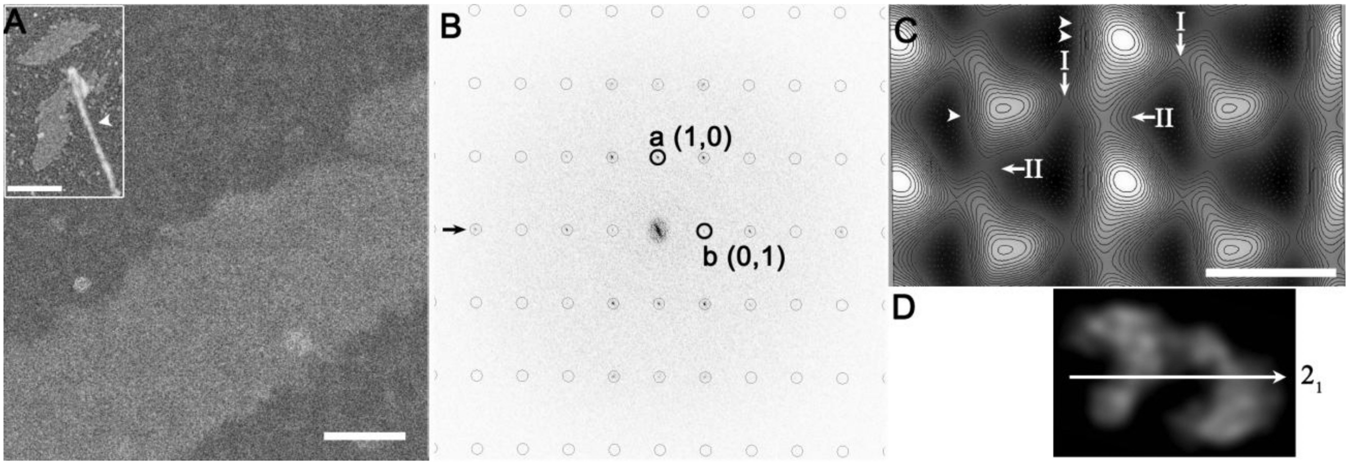

Fig. 1. Poliovirus 3Dpol planar lattices preserve interface-I contacts

(A) Purified 3Dpol self-assembled as planar sheets and tubular arrays. Negatively stained 3Dpol shows a regular rectangular pattern, which is best observed by viewing the image at a glancing angle. Scale bar 100 nm. Inset scale bar 500 nm. Arrow head points to a tubular array. (B) The power spectrum of a central region of the image shown in panel (A) has visible diffraction spots to 20 $Å^{-1}$ (black arrow). (C) A projection map computed from one region of a 3Dpol planar lattice; continuous contour lines are overlaid on a gray-scale image. Densities of the two molecules in the unit cell are non-equivalent (double arrowhead: molecule with stronger density; single arrow head: weaker density). Representative interface-I locations are marked by vertical arrows and labeled ‘I’; interface-II locations are marked by horizontal arrows and labeled ‘II’. (D) A 2-D projection map of an interface-I dimer from PDB 1rdr, shown aligned with a unit cell in panel c. White arrow designates the 2_1 screw axis. Scale bar 50Å, for panels c and d.

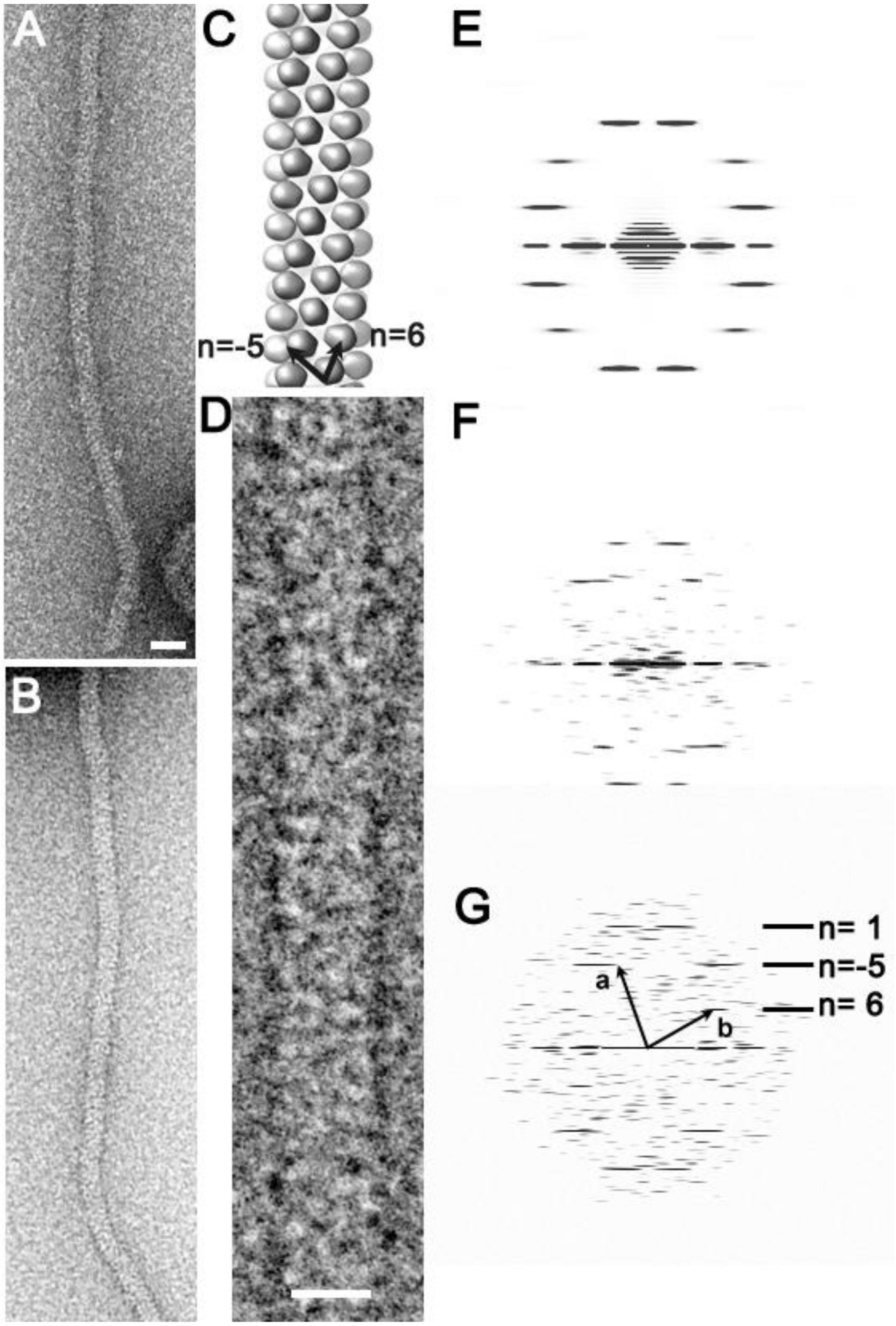

Fig. 2. Catalytically inactive 3Dpol has no interface-I contacts after oligomerization

(A) Narrow filament of wild-type 3Dpol was oligomerized by incubation at 4 °C. (B) Narrow filament of catalytic site mutant pol^{YGAA} oligomerized by incubation at 30 °C. Scale bar for (A) and (B), 200 Å. (C) A model of pol^{YGAA} filament from the (−5, 6) class: rise/subunit=6.7Å, rotation/subunit=63.3°, radius of the helix=50 Å. (D) A segment of spline-fitted pol^{YGAA} using tubuleJ [47]. Scale bar 100 Å. (E) Computed power spectrum of the simulated tube in C. (F) Power spectrum of a wild type 3Dpol tube oligomerized at 4 °C. (G) Power spectrum of pol^{YGAA} oligomerized at 30 °C. Major layerlines used for indexing are marked on the right margin.

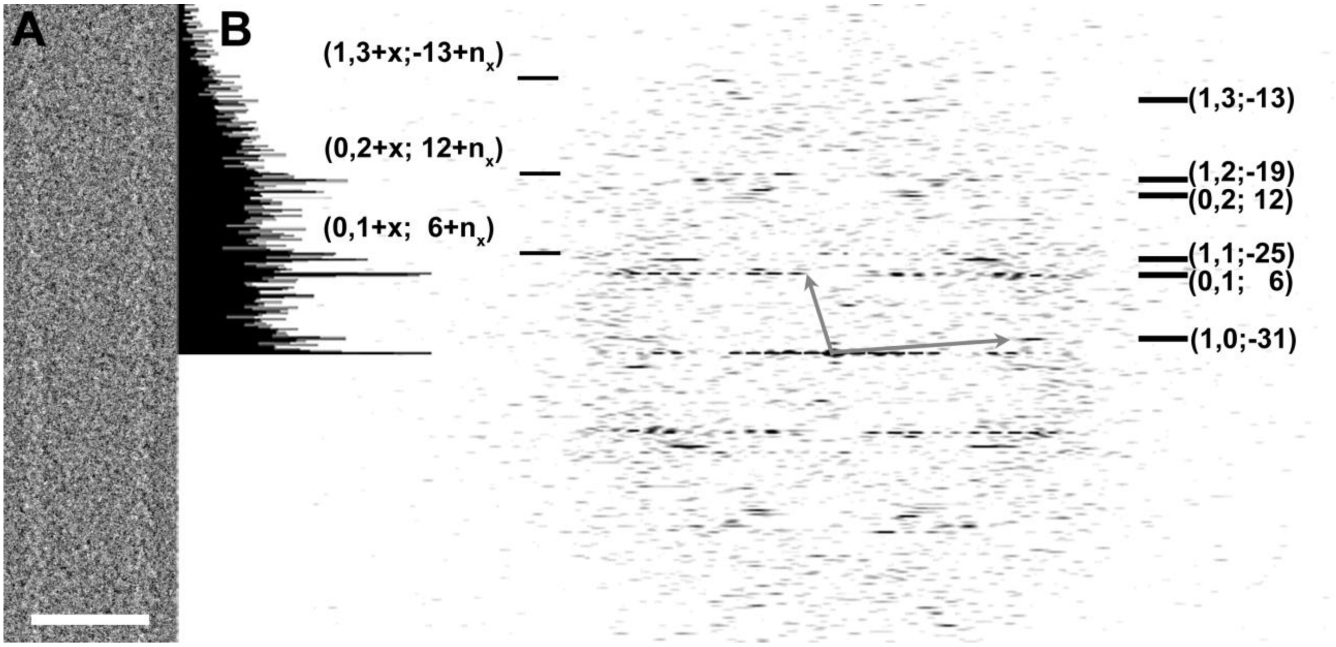

Fig. 3. Tubular crystals of poliovirus 3Dpol show helical symmetry plus ‘ghost’ layer lines

(A) Segment of a frozen hydrated tube of 3Dpol. Scale bar 500 Å. (B) Computed Fourier transform of the tube in (A) shows layer lines characteristic of helical structure, which are indexed to the right of the FT using their Miller indices h and k and Bessel order n, (h, k; n). Projection of the FT onto the y-axis is shown to the left of the FT. The unit cell of the helical lattice is marked by gray arrows. Strong ghost reflections (layer lines that are not accounted for by purely helical symmetry) are marked on the left margin, where x measures 1/5 the spacing of (1, 1), and correspondingly n_x =1/5 of the Bessel order $n_{1,1}$. Thus, for this tube from the (−31, 6) family, the visible ghost reflections have Bessel orders of 6+(−5)= −1; 12+(−5)=7; −13+(−5)= −18.

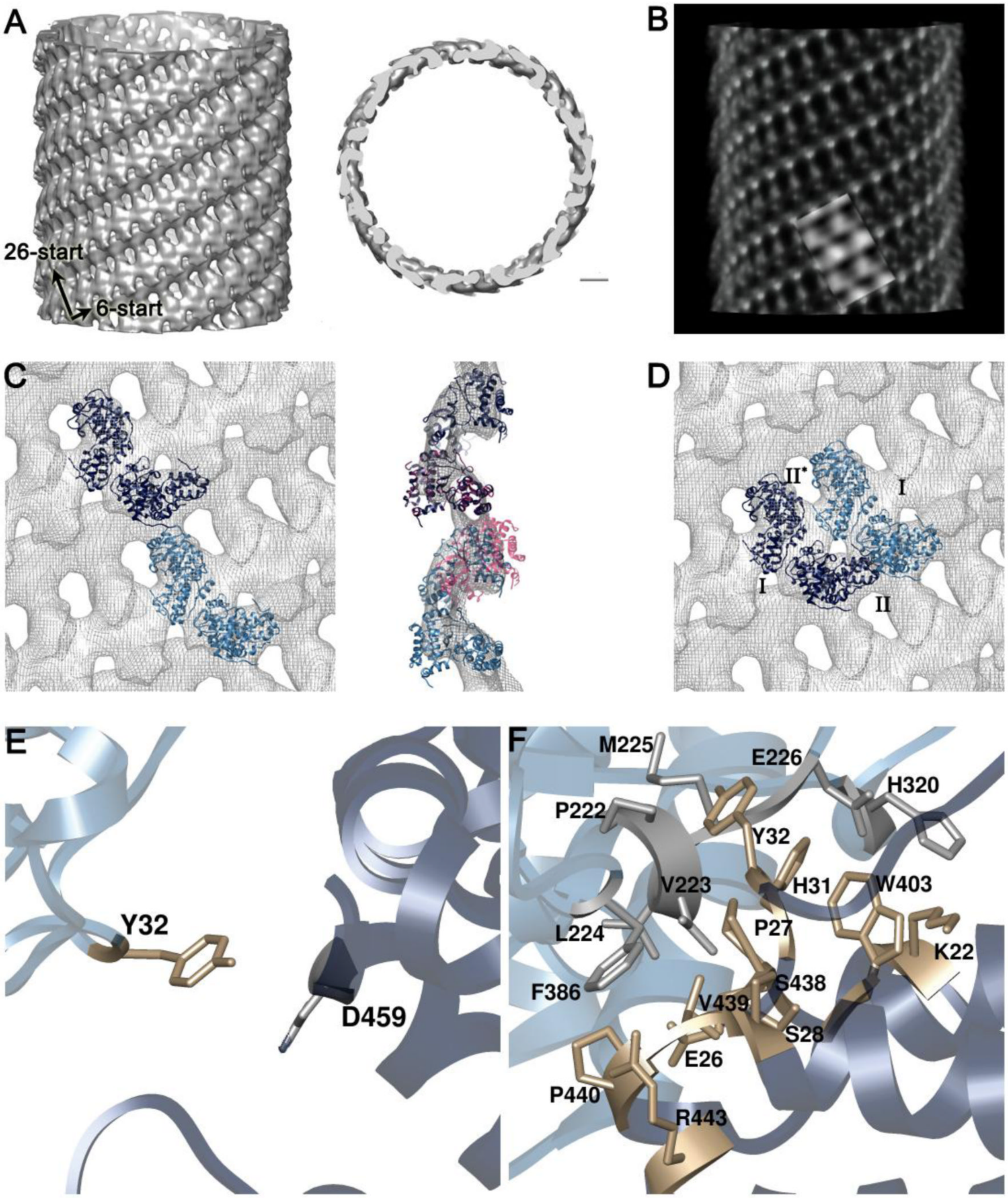

Fig. 4. Densities from two chemically identical polymerase molecules are not equivalent within the asymmetric unit of helical tubes of 3Dpol

(A) Surface maps of the (−32, 6) family of 3Dpol tubes. Black arrows point to the direction of the left-handed 26-start helices and the right-handed 6-start helices. Right panel: transverse section of the map, 50 Å thickness. Scale bar 50 Å. (B) A volume map of the reconstruction shown in grayscale. (C) Interface-I mediates the connection between weak and strong densities in the unit cell. A pair of interface-I dimers (1rdr) connected head-to-tail (light blue and dark blue) fit into the 26-start helical strand of 3Dpol reconstruction (mesh). Right panel: side view of the longitudinal section of the fitting. A third interface-I dimer (pink) reveals the change from of interface-I needed to fit the 26-start helical strand. (D)

Interface-I dimers docked side by side into a 6-start helix. Position of interface-I is marked as I; strong interface-II is marked by II, weak interface-II is marked by II*. (E & F) Residues involved in the weak (E) and strong (F) interface-II contacts.

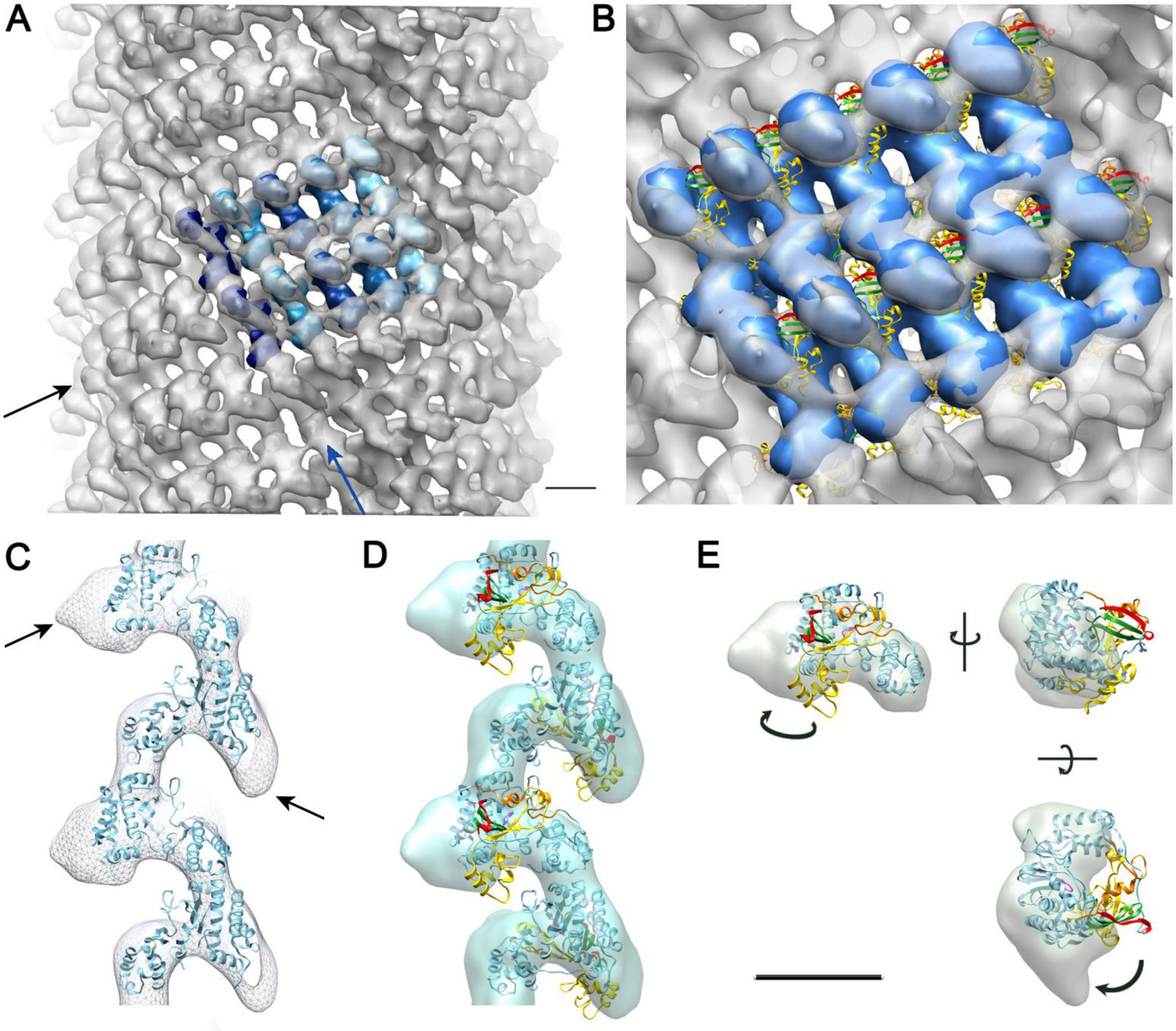

Fig. 5. Super-unit cells are revealed in helical tubes when ghost reflections are included

(A) The reconstruction of a tube belonging to the (−31, 6) family shows a super unit cell, bundling 5 copies of the asymmetric units to account for ghost reflections from the tube shown in Figure 3. Ten copies of the interface-I dimer (PDB 1rdr) illustrate two adjacent super unit cells. The hue of each dimer envelope corresponds to the value of its fit into the map, as measured by cross-correlation, with the darkest blue corresponding to the best fit. A 6-stranded helix is indicated by a black arrow and a 25-start helix is indicated by a blue arrow. Scale bar 50 Å. (B) The blue envelope encloses the density common to both the complete structure (1ra6) and the partial structure (1rdr). The fingers domain determined in the 1ra6 include residues 1–11 (red), 38–66 (orange), 98–180 (yellow) and 267–290 (green). (C) A cross-section along the 25-start helix with two interface-I dimer of the partial structure fitted in; black arrows mark densities at the tips of the outermost and innermost walls of the tube. (D) The fingers domain is not enclosed by the EM map of the tubular array. (E) A large conformational change (arrows) would be required to fit the crystal density of fingers domain into the EM map.

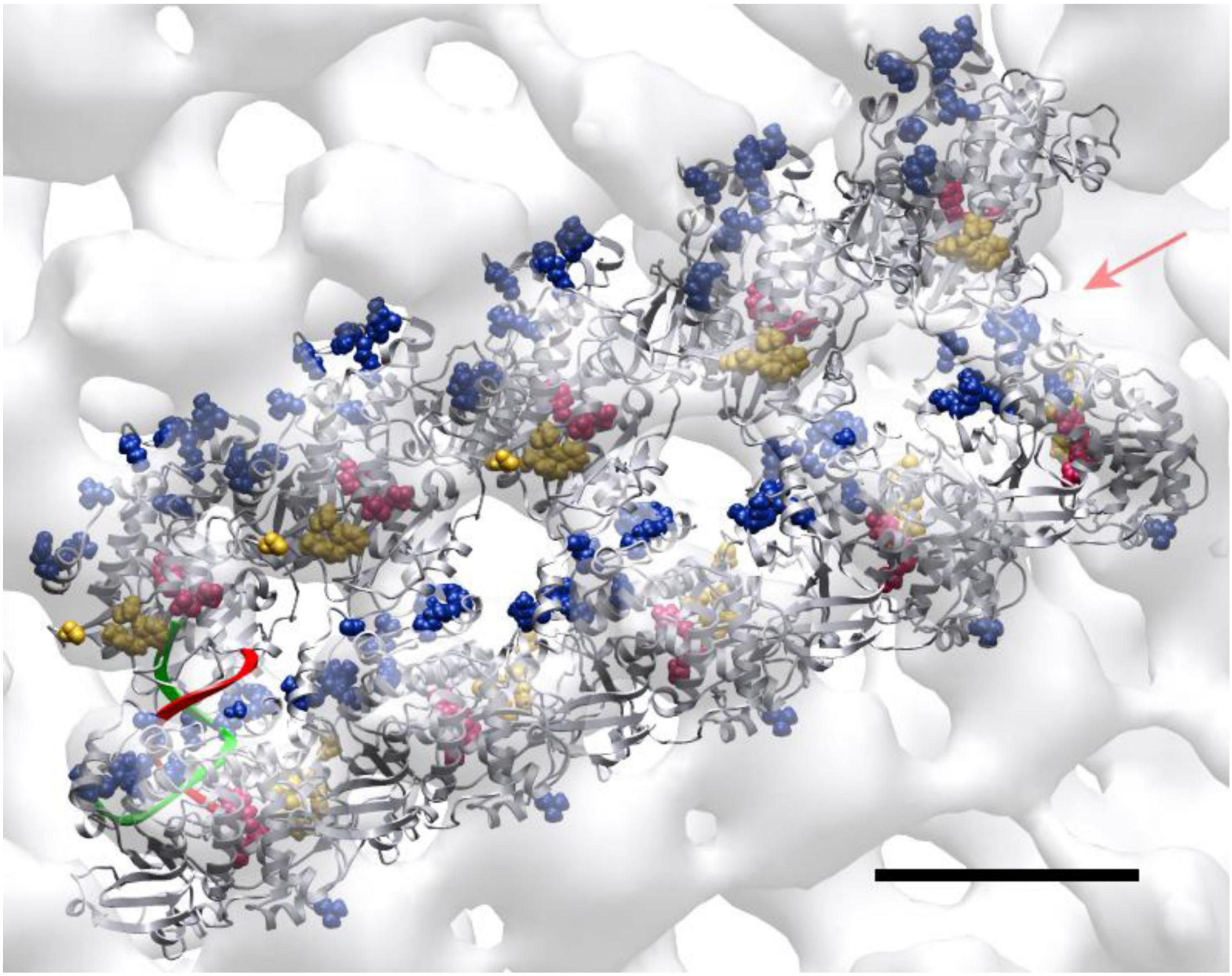

Fig. 6. Model for an RNA binding path within the 3Dpol lattice

3Dpol in complex with a short RNA duplex (PDB 3ol6) superposed onto an interface-I dimer and placed into the EM density map. For simplicity, only one such elongating RNA duplex is shown; template strand (red), newly synthesized strand (green). Residues shown to be involved in RNA binding are shown in blue, and include: K125, K126, K127, K128, K133, K188 [30]; R455, R456 [26]; L342, L446 [3]; the catalytic center shown in pink includes: Y326, G327, D328, D329; the Vpg binding site (yellow) includes F377, R379, E382 V391 [9;33]. The potential RNA binding path where the template strand can thread through is marked by the red arrow, and the template RNA would be moving in the direction of the arrow.

Table 1

Residues involved in interface-I interactions. The partial crystal structure 1rdr was fit into the EM map that included Ghost reflections; most finger interactions are not included since these residues were not visible in the crystal structure.

Interface-I Contacts				
Contact 1	Contact 2	Contact 3	Contact 4	Contact 5
337	337	337	313	313
337	339	339	337	339
338	342	341	339	340
338	345	342	340	341
339	444	345	341	342
339	446	348	342	345
345	449	363	345	411
345	452	437	348	415
451		444	363	443
		445	437	445
		446	443	446
		449	444	446
		455	445	447
			446	449
			447	452
			447	455
			449	
			452	
			455	

Table 2

Residues involved in interface-II interactions. The partial crystal structure 1rdr was fit into the EM map that included Ghost reflections; most finger interactions are not included since these residues were not visible in the crystal structure.

Interface-II Contacts					
Contact 1	Contact 2	Contact 3	Contact 4	Contact 5	Contact 6
24	26	25	25	24	32
25	381	26	26	25	384
26	382	27	27	26	
27	383	383	383	27	
312	384	384	384	381	
313	385	385	385	382	
314	386	386	386	383	
316	405	405		384	
334	406	406		385	
336	407	407		386	
339	408			403	
341	458			404	
342				405	
345				406	
346				407	
348					
349					
381					
382					
383					
384					
385					
386					
404					
405					
406					
407					

Interface-II Contacts
408
411
437
446
447
448
449
452
453
455
456
459